Rapid Communications

Resonant and bound states of charged defects in two-dimensional semiconductors

Martik Aghajanian,[1] Bruno Schuler,[2,*] Katherine A. Cochrane,[2] Jun-Ho Lee,[2,3] Christoph Kastl,[2,4] Jeffrey B. Neaton,[2,3,5] Alexander Weber-Bargioni,[2] Arash A. Mostofi,[1] and Johannes Lischner[1,†]

[1]*Department of Physics, Department of Materials, and the Thomas Young Centre for Theory and Simulation of Materials, Imperial College London, London SW7 2AZ, United Kingdom*

[2]*Molecular Foundry, Lawrence Berkeley National Laboratory, Berkeley, California 94720, USA*

[3]*Department of Physics, University of California at Berkeley, Berkeley, California 94720, USA*

[4]*Walter Schottky Institut and Physik Department, Technical University of Munich, Garching 85748, Germany*

[5]*Kavli Energy Nanosciences Institute at Berkeley, Berkeley, California 94720, USA*

(Received 15 August 2019; revised manuscript received 8 December 2019; accepted 6 February 2020; published 24 February 2020)

A detailed understanding of charged defects in two-dimensional semiconductors is needed for the development of ultrathin electronic devices. Here, we study negatively charged acceptor impurities in monolayer WS_2 using a combination of scanning tunneling spectroscopy and large-scale atomistic electronic structure calculations. We observe several localized defect states of hydrogenic wave function character in the vicinity of the valence band edge. Some of these defect states are bound, while others are resonant. The resonant states result from the multivalley valence band structure of WS_2, whereby localized states originating from the secondary valence band maximum at Γ hybridize with continuum states from the primary valence band maximum at K/K'. Resonant states have important consequences for electron transport as they can trap mobile carriers for several tens of picoseconds.

DOI: 10.1103/PhysRevB.101.081201

Impurity doping is the prime technology to control the electrical conductivity of semiconductors over several orders of magnitude [1,2]. Dopants introduce additional charge carriers that bind to the impurity and can be excited into the delocalized conduction or valence band states. Through this ionization process, the density of mobile charge carriers in the material is increased. However, the Coulomb potential induced by the positively charged donor or negatively charged acceptor scatters mobile charge carriers and thereby reduces carrier mobility. For this reason, it is usually desirable to eliminate any naturally occurring charged defects.

Importantly, the Coulomb potential of charged impurities is screened by the dielectric response of the host semiconductor. The resulting perturbation leads to the formation of localized Bloch states near the band edges [3]. For bulk semiconductors, such as silicon or gallium arsenide, these defect states have hydrogenic wave functions [4–7]. Because of the large dielectric constants and small effective masses of traditional bulk semiconductors, the wave functions extend over several nanometers and the corresponding binding energies are of the order of a few tenths of an electron volt [8]. These properties of charged defects are largely independent of their chemical origin and determined only by the long-ranged screened Coulomb potential induced by the impurity.

Many semiconductors exhibit multiple conduction or valence band valleys, i.e., their band structure features multiple extrema in the vicinity of the band gap. Such an electronic structure can result in the formation of *resonant impurity states* [9]. These states occur when a localized defect level originating from a secondary band extremum lies in the energy range of the continuum states of the primary band extremum [7]. The hybridization with the continuum states leads to an energy shift and a broadening of the localized level into a resonance. Such resonant defect states play an important role in transport properties [10–13] because a mobile charge carrier can be temporarily trapped by the impurity, reducing the carrier mobility [3].

Two-dimensional (2D) semiconductors, such as monolayer transition-metal dichalcogenides (TMDs), have been intensely studied over the last decade as promising candidates for nanoelectronic components, optoelectronic devices, and quantum information applications [14,15]. Understanding the properties of charged defects in these materials is a crucial step toward developing a viable route for impurity doping analogous to traditional (3D) semiconductors. A key difference between 2D and 3D semiconductors is their dielectric response to a charged perturbation. Specifically, the screened potential due to a point charge in 2D is not well-described by the bare Coulomb potential divided by a dielectric constant as in bulk semiconductors. Instead, in 2D semiconductors the dielectric response is relatively weak and highly anisotropic, giving rise to strongly bound excitons that dominate their optical response [16,17]. Unconventional screening of charged defects in monolayer TMDs with multivalley band structure and large spin-orbit effects can also give rise to bound defect states with unusual properties, e.g., the prediction that the most strongly bound acceptor state switches from being of K/K'-valley character to Γ-valley character at a critical value of the defect charge [18].

*bschuler@lbl.gov
†j.lischner@imperial.ac.uk

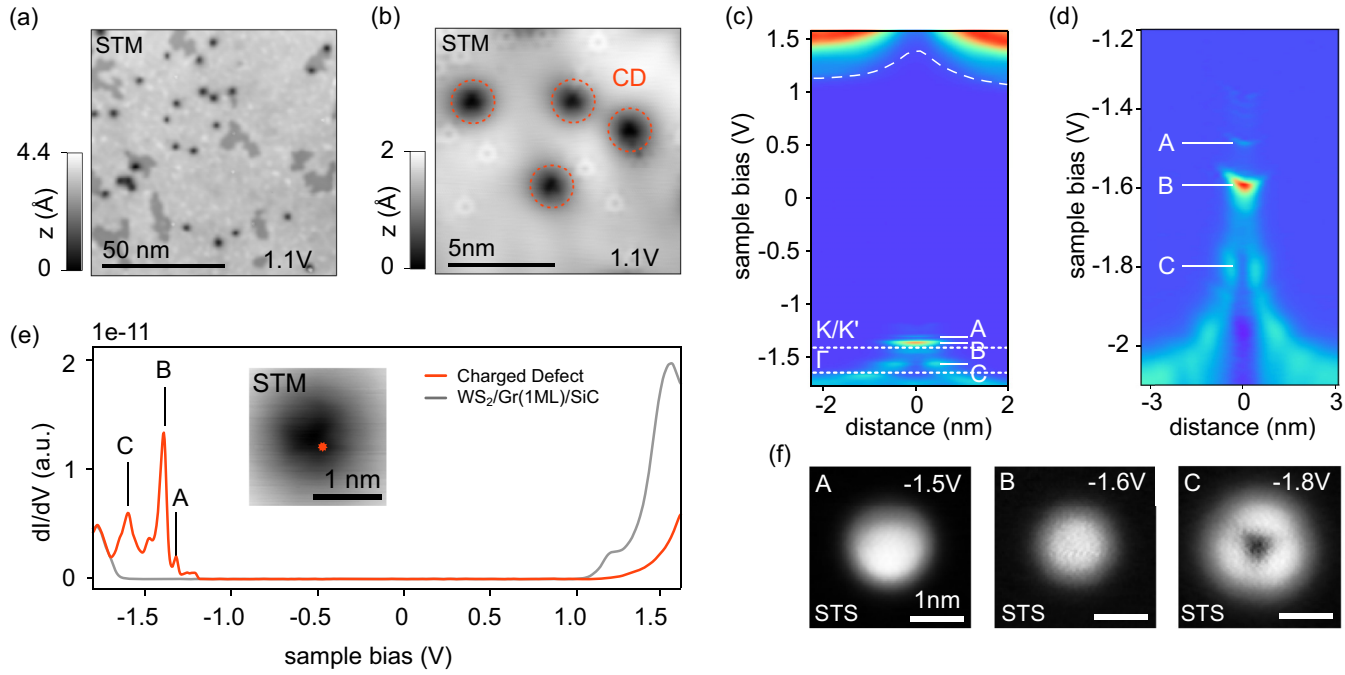

FIG. 1. (a) STM overview of the WS_2/graphene/SiC surface, $V_b = 1.1$ V. (b) STM image showing defects in WS_2. The charged defects (CDs) are indicated with a red circle. (c),(d) STS across a CD showing band bending and localized defect states labeled A, B, and C. In (c) the upward bending of the conduction band due to the negatively charged defect is indicated with a dashed white line, and the onset of the K/K' and Γ valleys of pristine WS_2 are indicated with white dotted lines. Note that the spectra in (c) and (d) were taken on different defects. (e) STS of a CD. (f) Constant height dI/dV maps of the defect corresponding to the electronic states A, B, and C.

In this Rapid Communication, we study the electronic properties of charged impurities in monolayer WS_2 on a graphene/SiC substrate using scanning tunneling microscopy/spectroscopy (STM/STS) and atomistic quantum-mechanical calculations. Using STS, we find that negatively charged impurities result in strong upwards band bending and a series of localized defect states near the valence band edge with *s*- and *p*-like character. Our calculations suggest that the *s*-like states are bound defect states originating from either the K/K' or Γ valleys, while the *p*-like states are resonant defect states resulting from the hybridization of localized states from the Γ valley with continuum states from the K/K' valleys. Finally, we discuss the relevance of these findings for transport devices.

STM/STS measurements were performed under ultrahigh vacuum at low temperature ($\sim$6 K). WS_2 samples were grown *ex situ* by chemical vapor deposition (CVD) on epitaxial graphene on silicon carbide substrates [19] and subsequent annealing in vacuum at $\sim$200 °C. A representative overview image of the surface is shown in Fig. 1(a). Even without intentional doping, we observe various point defects, including oxygen-in-sulfur substitutions (O_S), molybdenum-in-tungsten substitutions (Mo_W), and charged defects [20,21]. Charged defects, which we refer to as "CDs" can be readily distinguished from neutral defects by their characteristic STM contrast as seen in Figs. 1(a) and 1(b). CDs are among the most abundant point defects in our samples but their density varies considerably between different CVD preparations. Similar STM contrast has been observed in CVD-grown MoS_2 [22], metalorganic chemical vapor deposition– and molecular beam epitaxy (MBE) –grown WSe_2 [23,24], MBE-grown $MoSe_2$ [24], and natural bulk $MoS_2(0001)$ [25]. Some of these reports suggest that the observed defect might be charged [21,24,25] but their chemical origin remains unclear.

Using noncontact atomic force microscopy with a carbon monoxide (CO) functionalized tip [26] we previously revealed that the charged defect is a chalcogen substitution [21]. However, the chemical origin of the CDs has not yet been conclusively established. Possible candidates include a CH or N substitution at the S site [21]. These defects introduce unoccupied defect states in the band gap close to the valence band edge of WS_2 [see Supplemental Material (SM) [27]]. Since the Fermi level of the TMD/graphene/SiC heterostructure is pinned by the graphene/SiC substrate, formally unoccupied WS_2 defect states close to the valence band will be populated and hence become negatively charged. The graphene/SiC substrate acts like a Fermi sea filling (or depleting) all WS_2 defect states that are below (or above) the Fermi level [28], which resides in the upper half of the WS_2 band gap [29]. As the hybridization between the WS_2 states and the substrate is negligible [30], the impurity charge is an integer multiple of the electron charge.

In constant-current STM imaging, CDs are observed as large depressions at positive sample bias and protrusions at negative sample bias. This is an electronic effect: a negative charge located at the CD site results in local upwards band bending. As shown in the dI/dV spectra taken across a CD in Fig. 1(c), electrons are pushed to higher energies near the defect, leading to a position-dependent onset of the conduction band minimum (CBM), indicated with a white dashed line. The valence band of WS_2 exhibits two primary maxima at the K and K' points of the Brillouin zone and a secondary

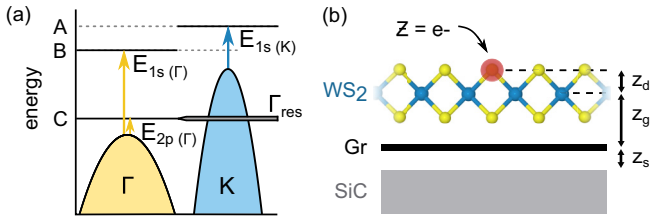

FIG. 2. (a) Schematic of the electronic structure of a negatively charged defect in WS_2. Shown are the primary valence band maximum at K (a second degenerate maximum exists at K') and the secondary maximum at Γ as well as the bound and resonant defect states. The states labeled $1s$ (K), $1s$ (Γ), and $2p$ (Γ) correspond to the experimental features A, B, and C in Fig. 1, respectively. (b) Schematic of the system consisting of a WS_2 layer on graphene on a silicon carbide substrate with a substitutional impurity with charge Z. Distances z_d, z_g, and z_s are indicated (see SM for details [27]).

maximum at the Γ point [see Fig. 2(a)]. The energies of these band extrema measured away from the defect are indicated by white dotted lines in Fig. 1(c). It should be noted that states originating from the K/K' point give only a weak STS signal. This is due to two factors: their relatively small effective mass results in a small local density of states (LDOS) and their large crystal momentum leads to a small tunneling matrix element [31]. In contrast, the larger effective mass and smaller crystal momentum at Γ results in a stronger STS signal.

While there are no observed defect states near the CBM, several defect resonances are observed at negative bias in the vicinity of the valence band edge [see Figs. 1(c) and 1(d)]. In Fig. 1(e), we have labeled the three dominant resonances as "A," "B," and "C." In addition, there are four very faint resonances observed just above state A (see SM [27]). We find that the localized defect states A and B lie on average 175 and 95 mV, respectively, above the onset of the K/K' valence band edge (see Table I), indicating that they are bound states. Resonance C lies 130 mV below the K/K' valence band edge, but 110 mV above the onset of the Γ valence band edge, suggesting that it is a resonant state, i.e., a localized state resonant with the continuum states from the K/K' valleys.

Spatially resolved dI/dV maps of the dominant states are shown in Fig. 1(f). A and B have a spherical shape reminiscent of an s-type orbital, whereas C has three lobes and a node at its center, indicative of a trigonally warped $2p$-type orbital [18]. With a lateral dimension of about 1.5–2 nm, the localized defect states are closely confined, as compared to the Rydberg states recently reported for ionized defects in bulk black phosphorus which extend more than 10 nm [32]. The smaller size of the acceptor states in our experiment is a consequence of the different environmental screening. Specifically, the metallic screening from the doped graphene substrate leads to more localized defect states compared to the states obtained for an insulating substrate.

TABLE I. Comparison of experimentally determined and theoretically calculated binding energies of three observed resonances: A, B, and C. Values are listed with respect to the K and Γ valence band edges. Positive binding energies indicate a lower energy with respect to the band edge.

	Experiment		Theory	
	K	Γ	K	Γ
A [$1s(K/K')$]/meV	+175	+415	+95	+355
B [$1s(\Gamma)$]/meV	+95	+335	+25	+285
C [$2p(\Gamma)$]/meV	−130	+110	−180	+80

To understand the experimental observations, we carried out theoretical calculations of acceptor impurities in WS_2 using a recently developed approach that allows the simulation of very large supercells [18]. In particular, we first calculated the screened potential of the defect, which is modeled as a point charge with $Z = -1$ located $z_d = 2.4$ Å above the plane of the tungsten atoms [see Fig. 2(b)]. For this, the dielectric function of the system is computed using the random phase approximation and the polarizability is expressed as the sum of contributions from the WS_2, the doped graphene, and the SiC substrate (see SM for details [27]).

To calculate the LDOS of a charged impurity in WS_2, we carry out large-scale tight-binding calculations using a three-band tight-binding model [33] with the screened defect potential included as an on-site energy [18]. This allows us to obtain converged results for a 45×45 WS_2 supercell. This supercell, which would be extremely challenging to model with *ab initio* techniques, is sufficiently large to capture the decay of the shallow impurity states and obtain accurate defect state energies. While this approach allows us to describe states induced by the long-ranged screened defect potential, the model does not capture short-ranged chemical interactions that could give rise to additional defect states.

Figures 3(a) and 3(b) show the calculated LDOS of an acceptor impurity in WS_2. In agreement with the measured dI/dV map [Fig. 1(c)], we observe a significant defect-induced upward bending of the conduction band edge. In the vicinity of the valence band edge, a series of defect states are found. Figure 3(c) shows the simulated STS images of the three most strongly bound defect states that give rise to significant peaks in the LDOS (see SM for details [27]). The two lowest energy states appear similar to experimental states A and B as circular bright spots with a similar size [Fig. 1(f)]. The energy differences with respect to the valence band maximum at K/K' of these states are 95 and 25 meV, respectively. While these values are somewhat smaller than the experimental ones (see Table I), their difference (70 meV) is in good agreement with experiment (80 meV). As these states exhibit symmetries similar to the eigenstates of the two-dimensional hydrogen atom, we label them as $1s$ states. Counterintuitively, we find that the lower energy $1s$ state is less localized than the other $1s$ state. At higher energies, a $2p$-like defect state is found that is characterized by a node at its center. This state resembles the experimental state C in Fig. 1(f). Its energy with respect to the primary valence band maximum at K is −180 meV indicating that it lies between Γ and K/K'. Again, we find that the energy difference between this state and the less strongly bound $1s$ state is in good agreement with experiment.

To understand which band extrema these defect states originate from, we decompose the defect wave functions into contributions from unperturbed WS_2 states. Figure 3(d) shows

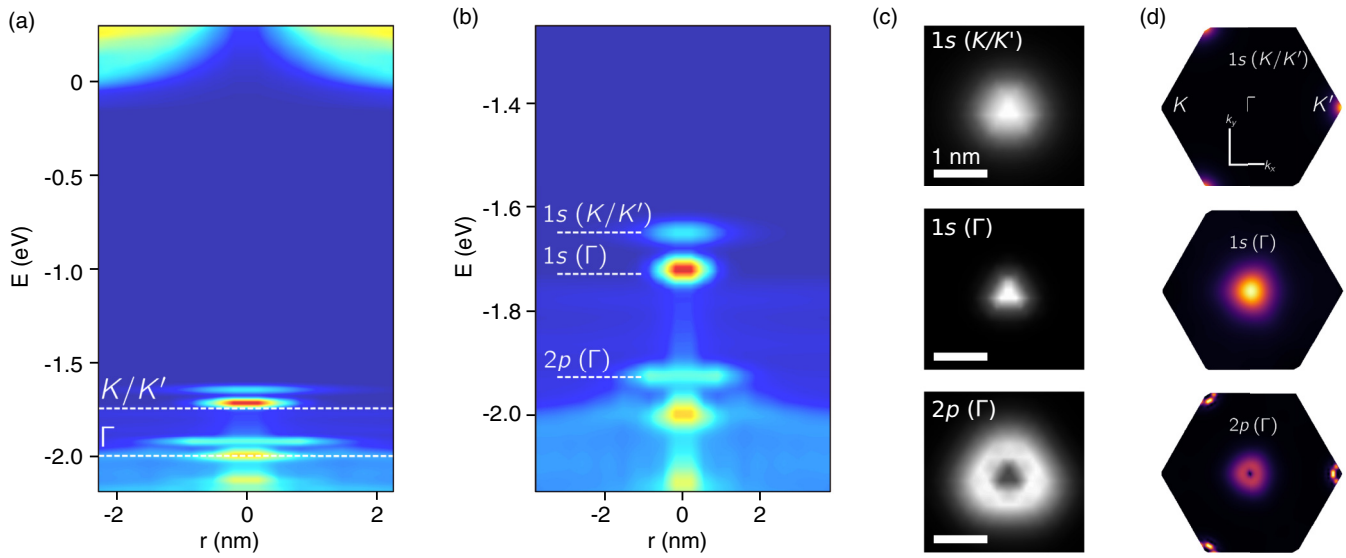

FIG. 3. (a),(b) Calculated local density of states of a negatively charged defect in WS_2 on graphene/SiC substrate. In (a), the onset of the K/K' and Γ valleys are indicated by dashed lines. In (b), the defect states are labeled by their hydrogenic quantum numbers and valley. (c) Simulated STS images of defect states. (d) Projections of defect wave functions onto unperturbed WS_2 states.

that the lowest energy defect state originates from the K valley (a second degenerate state with opposite spin originates from the K' valley) and is labeled as $1s$ (K), while the other $1s$ state originates from the Γ valley. Even though the $1s$ (Γ) state resides less deep in the band gap, its effective binding energy with respect to the relevant Γ band edge is greater than that of the $1s$ (K) state [see Fig. 2(a)]. Consequently, the wave function of the $1s$ (Γ) state is more confined, reestablishing the general anticorrelation between binding energy and spatial extent. The larger binding energies associated with states originating from the Γ valley is a direct consequence of its larger effective mass. The analysis of the $2p$ resonance reveals that this impurity level mostly originates from unperturbed states in the vicinity of Γ, but also has contributions from a few states near K (note that mixing only occurs between states with the same spin preventing any hybridization with states from K'). The valley hybridization results from the resonant nature of the $2p$ defect state and can be understood within the framework of effective mass theory [3]. In this approach, one first neglects the coupling between different valleys and obtains a set of bound defect states for each valley. When the coupling between valleys is turned on, the bound states from the secondary valence band extremum at Γ that lie in the same energy range as continuum states from the K and K' valleys can mix with the continuum states. The resulting hybridized states can be expressed as

$$\psi_{2p(\Gamma)}(\mathbf{r}) = c_{2p(\Gamma)}\phi_{2p(\Gamma)}(\mathbf{r}) + \sum_{n\in\{K,K'\}}\int_{\Omega_n} d\mathbf{k}\, c_n(\mathbf{k})\phi_{n\mathbf{k}}(\mathbf{r}), \qquad (1)$$

where $\phi_{2p(\Gamma)}$ and $\phi_{n\mathbf{k}}$ denote the bound and continuum states obtained for decoupled valleys, respectively (with n labeling the valley), $c_{2p(\Gamma)}$ and $c_n(\mathbf{k})$ are complex coefficients, and Ω_n denotes the k-space region corresponding to the nth valley.

Finally, we discuss the effect of resonant impurities on electron transport. If a hole near a primary band extrema (i.e., in the K or K' valley) in an external electric field reaches the energy of the resonant impurity state $E_{2p(\Gamma)}$, it does not participate in conduction for a time $\tau_{\text{res}} = \hbar\Gamma_{\text{res}}^{-1}$. Here, Γ_{res} denotes the width of the resonant impurity level given by

$$\Gamma_{\text{res}} = \pi \sum_{n\in\{K,K'\}}\int_{\Omega_n} d\mathbf{k}|V_{2p(\Gamma),n\mathbf{k}}|^2\delta(E_{2p(\Gamma)} - \epsilon_{n\mathbf{k}}), \qquad (2)$$

where $\epsilon_{n\mathbf{k}}$ denotes the energy of a continuum state with crystal momentum $\mathbf{k}$ in valley n and $V_{2p(\Gamma),n\mathbf{k}}$ is the matrix element of the Bloch-transformed screened impurity potential between $\phi_{2p(\Gamma)}(\mathbf{r})$ and $\phi_{n\mathbf{k}}(\mathbf{r})$ [3]. Evaluating this expression with our first-principles defect potential and tight-binding wave functions yields $\Gamma_{\text{res}} = 0.02$ meV and $\tau_{\text{res}} = 30$ ps. This result shows that resonant defect states exhibit extremely small linewidths corresponding to long trapping times. Thus, we predict that resonant states should lead to a drastic reduction in conductivity when the Fermi level reaches the resonant impurity level. Note that in a WS_2 transport device, graphene could not be used as substrate as most carriers would propagate through the graphene. Without graphene, the screening of the impurity charge would be reduced, resulting in a resonant impurity level that lies closer to the valence band maximum (VBM) at K/K'. The trapping time, however, would not change significantly because of the flat density of state of WS_2 near the VBM.

In this Rapid Communication, we examined the localized acceptor states associated with negatively charged point defects in WS_2 using scanning tunneling microscopy and spectroscopy. We identify these states as resonant and bound hydrogenic states of the screened Coulomb potential, which are to a large extent independent of the chemical impurity species. Our large-scale atomistic electronic structure calculations reproduce the band bending and binding energies of the defect states as well as their wave-function shapes and sizes as observed in STS measurements. The hydrogenic states exhibit s- and p-type character and originate

from both the K/K' and Γ valence band valleys. Despite the hybridization with the primary valence band around K and K', a resonant state emerging from Γ is clearly resolved. We further predict that resonant states can trap mobile carriers for up to 30 ps, impairing the mobility of transport devices. These insights provide a framework to understand the physics of hydrogenic bound defect states associated with charged defects naturally present in TMDs, guiding future efforts in chemical doping of TMDs and other two-dimensional semiconductors.

ACKNOWLEDGMENTS

This work was supported through a studentship in the Centre for Doctoral Training on Theory and Simulation of Materials at Imperial College London funded by the EPSRC (EP/L015579/1). We acknowledge the Thomas Young Centre under Grant No. TYC-101. With the support of J.L.'s membership of the UK's HEC Materials Chemistry Consortium, which is funded by EPSRC (EP/L000202, EP/R029431), this work used the ARCHER UK National Supercomputing Service. The work performed at the Molecular Foundry was supported by the Office of Science, Office of Basic Energy Sciences, of the US Department of Energy under Contract No. DE-AC02-05CH11231. B.S. appreciates support from the Swiss National Science Foundation under Project No. P2SKP2_171770. A.W.-B. was supported by the US Department of Energy Early Career Award. J.-H.L. and J.B.N. were supported by the Air Force Office of Scientific Research Hybrid Materials MURI under Award No. FA9550-18-1-0480. Computational resources for performing the *ab initio* calculations were provided by the National Energy Research Scientific Computing Center and the Molecular Foundry, DOE Office of Science User Facilities supported by the Office of Science of the US Department of Energy under Contract No. DE-AC02-05CH11231.

[1] J. Sun, Z. Yu, Y. Huang, Y. Xia, W. S. Lai, and H. Gong, Significant improvement in electronic properties of transparent amorphous indium zinc oxide through yttrium doping, Europhys. Lett. **106**, 17006 (2014).

[2] C. G. Van de Walle, J. L. Lyons, and A. Janotti, Controlling the conductivity of InN, Phys. Status Solidi A **207**, 1024 (2010).

[3] F. Bassani, G. Iadonisi, and B. Preziosi, Electronic impurity levels in semiconductors, Rep. Prog. Phys. **37**, 1099 (1974).

[4] Z. Xie, Y. Sui, J. Buckeridge, C. R. A. Catlow, T. W. Keal, P. Sherwood, A. Walsh, D. O. Scanlon, S. M. Woodley, and A. A. Sokol, Demonstration of the donor characteristics of Si and O defects in GaN using hybrid QM/MM, Phys. Status Solidi A **214**, 1600445 (2017).

[5] G. Zhang, A. Canning, N. Grønbech-Jensen, S. Derenzo, and L.-W. Wang, Shallow Impurity Level Calculations in Semiconductors Using *ab initio* Methods, Phys. Rev. Lett. **110**, 166404 (2013).

[6] G. Bastard, Hydrogenic impurity states in a quantum well: A simple model, Phys. Rev. B **24**, 4714 (1981).

[7] S. Z. Karazhanov, Y. Zhang, L.-W. Wang, A. Mascarenhas, and S. Deb, Resonant defect states and strong lattice relaxation of oxygen vacancies in WO_3, Phys. Rev. B **68**, 233204 (2003).

[8] W. Kohn, Shallow impurity states in silicon and germanium, Solid State Phys. **5**, 257 (1957).

[9] S. G. Louie, M. Schlüter, J. R. Chelikowsky, and M. L. Cohen, Self-consistent electronic states for reconstructed Si vacancy models, Phys. Rev. B **13**, 1654 (1976).

[10] H. Yu, A. R. Shaikh, F. Xiong, and Y. Chen, Enhanced out-of-plane electrical transport in n-type SnSe thermoelectrics induced by resonant states and charge delocalization, ACS Appl. Mater. Interfaces **10**, 9889 (2018).

[11] Q. Zhang, H. Wang, W. Liu, H. Wang, B. Yu, Q. Zhang, Z. Tian, G. Ni, S. Lee, K. Esfarjani, G. Chen, and Z. Ren, Enhancement of thermoelectric figure-of-merit by resonant states of aluminium doping in lead selenide, Energy Environ. Sci. **5**, 5246 (2012).

[12] K. Szlenk, Z. Dziuba, and R. Galazka, Contribution of resonant states to the conductivity of HgTe, Phys. Status Solidi B **91**, 255 (1979).

[13] J. Stankiewicz and W. Giriat, Galvanomagnetic properties of pure HgTe under high hydrostatic pressure, Phys. Rev. B **13**, 665 (1976).

[14] A. Kormányos, V. Zólyomi, N. D. Drummond, and G. Burkard, Spin-Orbit Coupling, Quantum Dots, and Qubits in Monolayer Transition Metal Dichalcogenides, Phys. Rev. X **4**, 011034 (2014).

[15] B. W. H. Baugher, H. O. H. Churchill, Y. Yang, and P. Jarillo-Herrero, Optoelectronic devices based on electrically tunable p-n diodes in a monolayer dichalcogenide, Nat. Nanotechnol. **9**, 262 (2014).

[16] K. F. Mak, C. Lee, J. Hone, J. Shan, and T. F. Heinz, Atomically Thin MoS_2: A New Direct-Gap Semiconductor, Phys. Rev. Lett. **105**, 136805 (2010).

[17] D. Y. Qiu, F. H. da Jornada, and S. G. Louie, Optical Spectrum of MoS_2: Many-Body Effects and Diversity of Exciton States, Phys. Rev. Lett. **111**, 216805 (2013).

[18] M. Aghajanian, A. A. Mostofi, and J. Lischner, Tuning electronic properties of transition-metal dichalcogenides via defect charge, Sci. Rep. **8**, 13611 (2018).

[19] C. Kastl, C. T. Chen, T. Kuykendall, B. Shevitski, T. P. Darlington, N. J. Borys, A. Krayev, P. J. Schuck, S. Aloni, and A. M. Schwartzberg, The important role of water in growth of monolayer transition metal dichalcogenides, 2D Mater. **4**, 021024 (2017).

[20] S. Barja, S. Refaely-Abramson, B. Schuler, D. Y. Qiu, A. Pulkin, S. Wickenburg, H. Ryu, M. M. Ugeda, C. Kastl, C. Chen, C. Hwang, A. Schwartzberg, S. Aloni, O. D. F. Mo, Sung-Kwan, M. F. Crommie, O. V. Yazyev, S. G. Louie, J. B. Neaton, and A. Weber-Bargioni, Identifying substitutional oxygen as a prolific point defect in monolayer transition metal dichalcogenides with experiment and theory, Nat. Commun. **10**, 3382 (2019).

[21] B. Schuler, J.-H. Lee, C. Kastl, K. A. Cochrane, C. T. Chen, S. Refaely-Abramson, S. Yuan, E. van Veen, R. Roldan, N. J. Borys *et al.*, How substitutional point defects in two-dimensional WS_2 induce charge localization, spin–orbit splitting, and strain, ACS Nano **13**, 10520 (2019).

[22] X. Liu, I. Balla, H. Bergeron, and M. C. Hersam, Point defects and grain boundaries in rotationally commensurate MoS_2 on epitaxial graphene, J. Phys. Chem. C. **120**, 20798 (2016).

[23] Y.-C. Lin, B. Jariwala, B. M. Bersch, K. Xu, Y. Nie, B. Wang, S. M. Eichfeld, X. Zhang, T. H. Choudhury, Y. Pan *et al.*, Realizing large-scale, electronic-grade two-dimensional semiconductors, ACS Nano **12**, 965 (2018).

[24] T. Le Quang, K. Nogajewski, M. Potemski, M. T. Dau, M. Jamet, P. Mallet, and J. Veuillen, Band-bending induced by charged defects and edges of atomically thin transition metal dichalcogenide films, 2D Mater. **5**, 035034 (2018).

[25] R. Addou, L. Colombo, and R. M. Wallace, Surface defects on natural MoS_2, ACS Appl. Mater. Interfaces **7**, 11921 (2015).

[26] L. Gross, F. Mohn, N. Moll, P. Liljeroth, and G. Meyer, The chemical structure of a molecule resolved by atomic force microscopy, Science **325**, 1110 (2009).

[27] See Supplemental Material http://link.aps.org/supplemental/10.1103/PhysRevB.101.081201 for additional details, which includes Refs. [34–41].

[28] M. Brotons-Gisbert, A. Branny, S. Kumar, R. Picard, R. Proux, M. Gray, K. S. Burch, K. Watanabe, T. Taniguchi, and B. D. Gerardot, Coulomb blockade in an atomically thin quantum dot coupled to a tunable fermi reservoir, Nat. Nanotechnol. **14**, 442 (2019).

[29] C. Kastl, C. Chen, R. J. Koch, B. Schuler, T. Kuykendall, A. Bostwick, C. Jozwiak, T. Seyller, E. Rotenberg, A. Weber-Bargioni *et al.*, Multimodal spectromicroscopy of monolayer WS_2 enabled by ultra-clean van der Waals epitaxy, 2D Mater. **5**, 045010 (2018).

[30] B. Schuler, D. Y. Qiu, S. Refaely-Abramson, C. Kastl, C. T. Chen, S. Barja, R. J. Koch, D. F. Ogletree, S. Aloni, A. M. Schwartzberg *et al.*, Large Spin-Orbit Splitting of Deep In-Gap Defect States of Engineered Sulfur Vacancies in Monolayer WS_2, Phys. Rev. Lett. **123**, 076801 (2019).

[31] Y. Zhang, V. W. Brar, F. Wang, C. Girit, Y. Yayon, M. Panlasigui, A. Zettl, and M. F. Crommie, Giant phonon-induced conductance in scanning tunnelling spectroscopy of gate-tunable graphene, Nat. Phys. **4**, 627 (2008).

[32] Z. Qiu, H. Fang, A. Carvalho, A. Rodin, Y. Liu, S. J. Tan, M. Telychko, P. Lv, J. Su, Y. Wang *et al.*, Resolving the spatial structures of bound hole states in black phosphorus, Nano Lett. **17**, 6935 (2017).

[33] G. Liu, D. Xiao, Y. Yao, X. Xu, and W. Yao, Electronic structure and theoretical modelling of two-dimensional group-VIB transition metal dichalcogenides, Chem. Soc. Rev. **44**, 2643 (2015).

[34] J. Deslippe, G. Samsonidze, D. A. Strubbe, M. Jain, M. L. Cohen, and S. G. Louie, Berkeleygw: A massively parallel computer package for the calculation of the quasiparticle and optical properties of materials and nanostructures, Comput. Phys. Commun. **183**, 1269 (2012).

[35] K. V. Emtsev, A. Bostwick, K. Horn, J. Jobst, G. L. Kellogg, L. Ley, J. L. McChesney, T. Ohta, S. A. Reshanov, J. Röhrl, E. Rotenberg, A. K. Schmid, D. Waldmann, H. B. Weber, and T. Seyller, Towards wafer-size graphene layers by atmospheric pressure graphitization of silicon carbide, Nat. Mater. **8**, 203 (2009).

[36] B. Wunsch, T. Stauber, F. Sols, and F. Guinea, Dynamical polarization of graphene at finite doping, New J. Phys. **8**, 318 (2006).

[37] S. Ismail-Beigi, Truncation of periodic image interactions for confined systems, Phys. Rev. B **73**, 233103 (2006).

[38] I. Hamada, van der Waals density functional made accurate, Phys. Rev. B **89**, 121103(R) (2014).

[39] D. Y. Qiu, F. H. da Jornada, and S. G. Louie, Screening and many-body effects in two-dimensional crystals: Monolayer MoS_2, Phys. Rev. B **93**, 235435 (2016).

[40] H.-J. Kim, S.-H. Kang, I. Hamada, and Y.-W. Son, Origins of the structural phase transitions in $MoTe_2$ and WTe_2, Phys. Rev. B **95**, 180101(R) (2017).

[41] L. Patrickand W. Choyke, Static dielectric constant of SiC, Phys. Rev. B **2**, 2255 (1970).